Chapter 6

AlGaAs/GaAs Quantum Well Infrared Photodetectors

Michael A. Dem'yanenko, Dmitry G. Esaev, Aleksandr I. Toropov, Natalia A. Valisheva, Sergey A. Dvoretsky, Dmitry V. Dmitriev, Dmitry V. Gulyaev, Vladimir A. Fateev, Igor V. Marchishin, Dmitry Yu Protasov, Anatoly P. Savchenko, Victor N. Ovsyuk and Konstantin Zhuravlev

Additional information is available at the end of the chapter

http://dx.doi.org/10.5772/intechopen.71266

Abstract

In this article, we present an overview of a focal plane array (FPA) with 640 × 512 pixels based on the AlGaAs quantum well infrared photodetector (QWIP). The physical principles of the QWIP operation and their parameters for the spectral range of 8–10 μm have been discussed. The technology of the manufacturing FPA based on the QWIP structures with the pixels 384 × 288 and 640 × 512 has been demonstrated. The parameters of the manufactured 640 × 512 FPA with a step of 20 μm have been given. At the operating temperature of 72 K, the temperature resolution of QWIP focal plane arrays is less than 35 mK. The number of defective elements in the matrix does not exceed 0.5%. The stability and uniformity of the FPA have been demonstrated.

Keywords: GaAs/AlGaAs quantum well infrared photodetector, focal plane array, multiplexer, dark current, noise equivalent temperature difference

1. Introduction

The solution to a well-known problem of a finite rectangular quantum well (QW) indicates that the energy position of the quantum subbands is determined by several parameters, namely, the width of the quantum well, the height of the barriers, and the carrier effective

masses. The possibility of a rather simple way of monitoring the wavelength of intersubband transitions in a quantum well to create photodetectors has attracted the attention of researchers for a long time [1]. Improving the technology of the molecular beam epitaxy (MBE) has allowed converting these dreams into reality. The quantum well infrared photodetector (QWIP) was first demonstrated on the basis of the AlGaAs/GaAs heterostructure in 1987 [2]. Permanent improvement of the QWIP design, epitaxial growth technologies of the AlGaAs layers, and techniques for device manufacturing allow using the QWIP based on AlGaAs/GaAs heterostructures not only for military purposes but also for various civilian tasks [3–7].

In this paper, we have described the current state of the manufacturing technology in the Rzhanov Institute of Semiconductor Physics of SB RAS for the focal plane array (FPA) based on the AlGaAs/GaAs QWIP structure.

2. The physical model of the QWIP

A typical heterostructure intended to detect the infrared radiation (IR) is shown in **Figure 1**. Such heterostructures are commonly formed by a thin (4–6 nm) GaAs QW located between the wide band gap AlGaAs barrier layers. The thickness of these barrier layers (L_b) is much larger than the width (L_w) of the quantum well and selected in a range of 40–55 nm to suppress a dark current caused by the electron tunneling between the neighboring QWs. The barrier height ΔE_c is determined by the aluminum mole fraction (x) in the barriers. The energy position of the

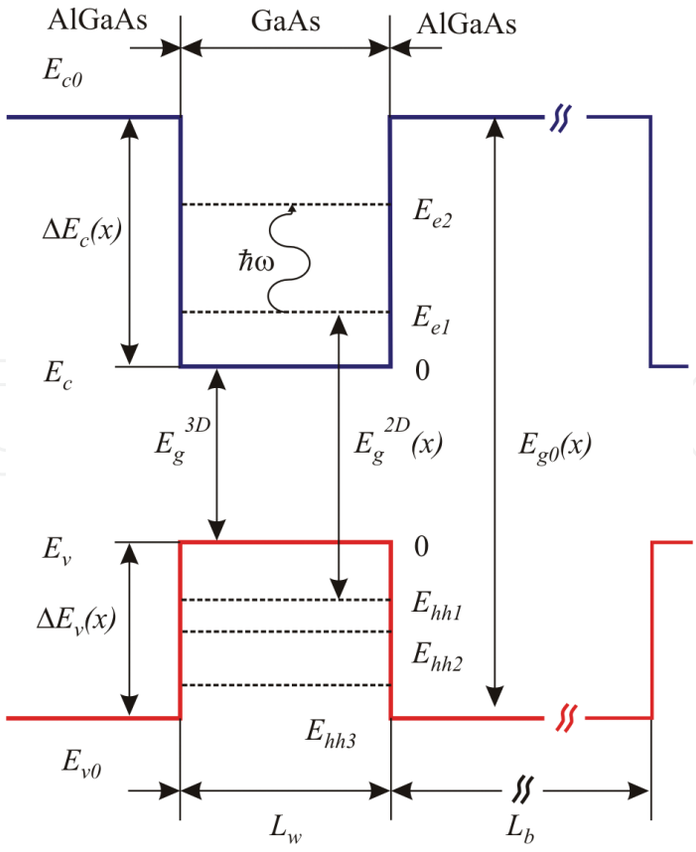

Figure 1. The energy structure of the GaAs/AlGaAs QW.

quantum levels depends not only on the quantum well thickness but also on x, as the barrier height is not infinite.

In such a structure, the electron moves from a ground quantum level *Ee1* to the first excited level *Ee2* at the absorption of the photon with the energy $\hbar\omega$. In contrast to the bulk case, the probability of intersubband transitions depends on the direction (polarization) of the electric field in the incident electromagnetic wave. In this case, the matrix element of the intersubband transition from the i-th level to the j-th level obtained in the first order of the perturbation theory is proportional $\langle jk'|e\cdot\widehat{p}|ik\rangle$ [8], where e is the polarization vector of a electromagnetic wave and $\widehat{\mathrm{p}}$ is the momentum operator. In case of the polarization of the electromagnetic wave in the QW plane (in x or y directions), the polarization vector is equal to $e=(1, 0, 0)$ or $e=(0, 1, 0)$, whereas the operator is equal to $-i\hbar\,\partial/\partial x$ or $-i\hbar\,\partial/\partial y$, respectively. Thus, under the influence of this operator upon the total wave function

$$\Psi_{ik}(R) = A^{-1/2}\phi_i(z)e^{ik\cdot r} \tag{1}$$

such expressions as $\hbar k_{x,y}\langle jk' \mid ik\rangle$ being zero at the $i \neq j$ resulted from the orthogonality of the wave functions are to be obtained. The constant A in the expression (Eq.(1)) is the area of the quantum well.

Conversely, when the electromagnetic wave is polarized along the z axis, the operator $e\widehat{p}$ is equal to $-i\hbar\,\partial/\partial z$ and the expression $\langle jk'|e\cdot\widehat{p}|ik\rangle$ changes as:

$$\langle jk'|e\cdot\widehat{p}|ik\rangle = -i\hbar A^{-1/2}\int \phi_j^*(z)\frac{\partial}{\partial z}\phi_i(z)dz\int e^{i(k-k')\cdot r}d^2r \tag{2}$$

The first integral in expression (Eq.(2)) is nonzero for i and j with different parities, and the last integral is nonzero for $k=k'$. Therefore, optical transitions in the QW occur only in the presence of polarization in an electromagnetic wave along the coordinate z, i.e., in the direction of the heterostructure growth.

The concentration of the two-dimensional electron gas (2DEG) in the photodetector structures should be large enough to locate the ground quantum level below the Fermi level. The required position of the Fermi level is achieved at the 2DEG concentration (N_{2D}) approximately equal to $(4-5)\times 10^{11}$ cm^{-2}. This electron density is distributed over the QW width in proportion to the square of the ground state wave function. According to the Poisson equation, such a large number of negative charges result in the appearance of a negative curvature of the conduction band bottom in the quantum well. It is worth mentioning that the middle part of the QW is maximally distorted, where the value of the square of the cosine is maximum. However, it is the middle part of the QW that is commonly doped to fill the QWs with electrons. A positive charge of the ionized donors bends the bottom of the QW back and downward. Consequently, the quantum wells remain almost rectangular shape under such a method of doping. The potential diagrams, the energy of the quantum levels, and wave functions in such rectangular AlGaAs/GaAs/AlGaAs quantum wells calculated by the *nextnano* program are shown **Figure 2A** [9].

The doping of the structure outside the GaAs QW (so-called the modulation-doped QWs) leads to significant changes in the QW shape (**Figure 2B**). Actually, the separation of electrons

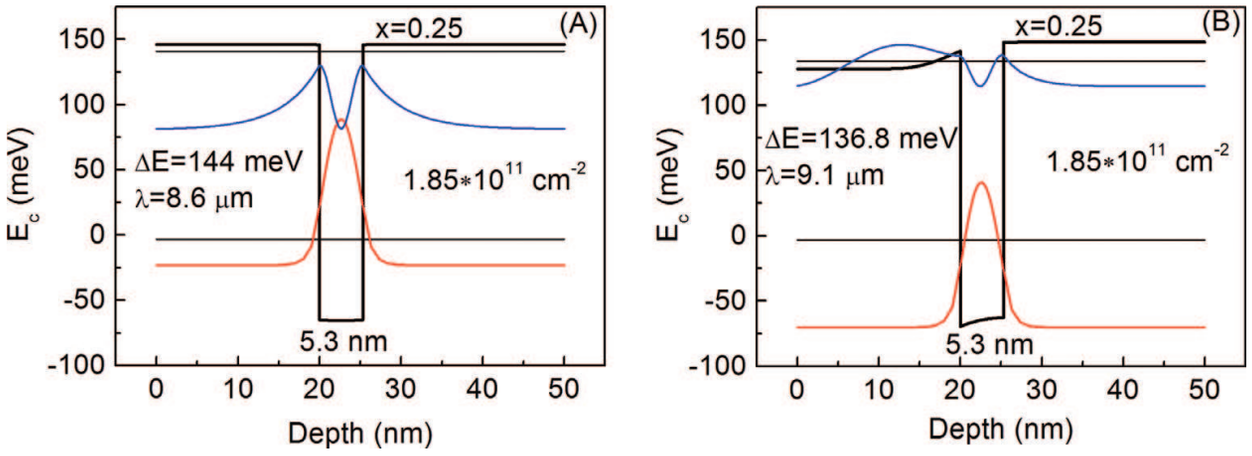

Figure 2. The calculated potential diagrams and wave functions for AlGaAs/GaAs/ AlGaAs QWs: (A) doped in the middle part of the quantum well; (B) with the one-side δ-doping with the 5-nm spacer.

and ionized donors causes the appearance of an electric field and, therefore, a noticeable bending of the band next to the quantum well region. Therefore, the energy of the quantum levels changes. The calculated energies of the ground and first-excited quantum levels resulted from a self-consistent calculation proved to be equal to 3.2/140.9 meV and −3.1/133.7 meV for the QW doped in middle part and the modulation-doped QW, respectively. These values are given with respect to the Fermi level that lies at the energy $\varepsilon = 0$. As one can easily estimate, the shift in the quantum levels resulted from the changes in the doping location leads to a shift in the intersubband absorption band by 0.5 μm.

The nomograms of the dependence of the intersubband transition line upon the QW width and the barrier height were calculated by the self-consistent solution of the Schrödinger and Poisson equations to compare the rectangular and modulation-doped QWs. **Figure 3** shows the calculated

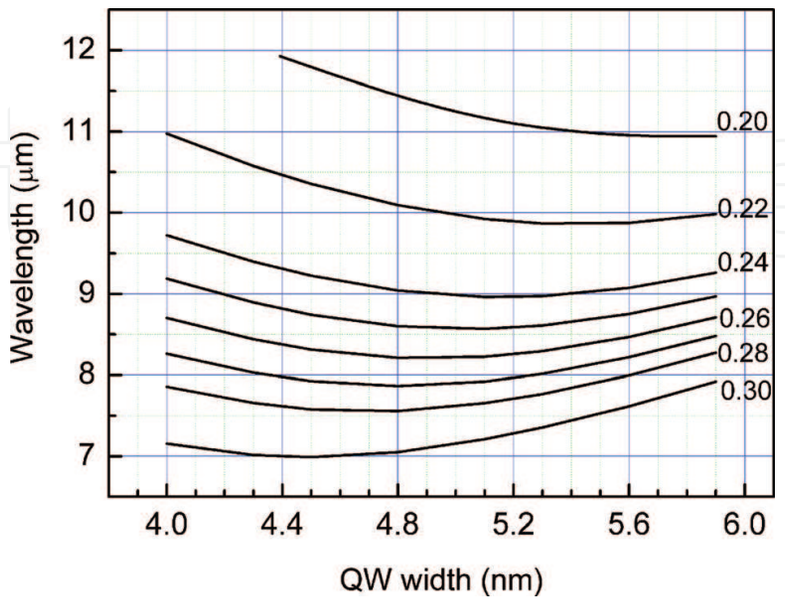

Figure 3. The nomogram showing the dependence of the wavelength upon the quantum well width and the barrier height (molar aluminum mole fraction) for a quantum well with the middle doped part.

nomogram for the QW doped in the middle part. As one can see from **Figure 3**, λmax is weakly dependent on the QW width in the wavelength region (8–10 μm) worth examining, whereas the required wavelength of the IR absorption is more difficult to obtain in the modulation-doped QWs. One more parameter is added, and the energy of the intersubband transition from the ground to the first excited level depends not only on the well width and the barrier height (or the Al mole fraction in the barrier) but also on the doping level. Therefore, the calculation was made for the modulated-doped QW at a fixed QW width equal to 5.6 nm (**Figure 4**).

The dark current flowing in the thermal equilibrium through the photodetector under a bias is an important characteristic of a QWIP. Its value is frequently used as a QWIP quality criterion. In QWIPs, the physical reason for the appearance of a dark current is the thermionic electron emission from the ground-filled quantum level to continuum states both above and below the energy barrier E_{c0} (**Figure 1**), due to its tunneling through the triangle barrier in the electric field.

The dark current density (I_d) in the structure shown in **Figure 1** consists of the thermoactivation and tunneling components, and it has the following general form [8]:

$$J(E) = q \cdot v(E) \left(\frac{m^*}{\pi \hbar^2 (L_W + L_B)} \right) \int_{\varepsilon_1}^{\infty} f(\varepsilon, T) T(\varepsilon, E) dE \tag{3}$$

where $v(E) = \mu E \sqrt{1 + \left({}^{\mu E}/_{v_{sat}} \right)^2}$ is the average electron drift velocity in the AlGaAs barrier layers, v_{sat} = 2.9×10^6 cm/s is the saturation velocity in the multiple quantum well (MQW), μ_n = 10^3 cm^2/V is the electron mobility in the AlGaAs with $x \approx 0.3$, ε_1 is the energy of the ground level in the quantum well. The fourth multiplier in (Eq. (3)) determines the concentration of the carriers participating in the conductivity, $f(\varepsilon)$ is the Fermi distribution function

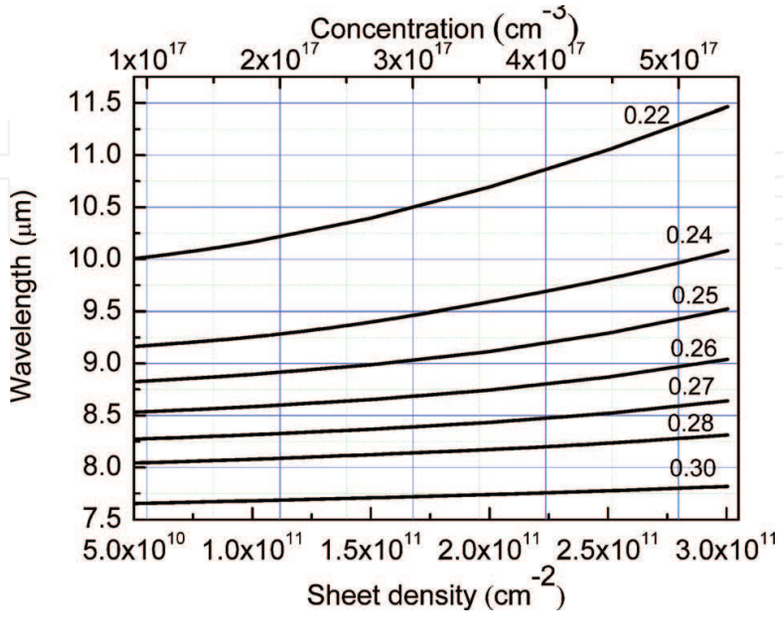

Figure 4. The nomogram showing the dependence of the wavelength upon the 2DEG concentration and the barrier height (aluminum mole fraction) in the modulation-doped QWs.

of the 2DEG, and $T(\varepsilon,E)$ is the probability of tunneling of the electrons from the GaAs layer to the states above the barrier. The electric field dependence of the $T(\varepsilon,E)$ reflects the effective barrier lowering for the hot electrons with a total energy $\varepsilon \cong V_b$. We can assume with good accuracy that for $\varepsilon > V_{b,}$ the coefficient is $T(\varepsilon,E) \approx 1$, whereas for $\varepsilon < V_{b,}$ the coefficient is $T(\varepsilon,E) = 0$.

The modeling with the help of *nextnano* has shown that the barrier lowering in an electric field can be well described by the expression:

$$V_b(E) = V_b^0 - qE\frac{L_W}{2} \tag{4}$$

Thus, the current density through the heterostructure is finally obtained as:

$$j(E) = q{\cdot}\nu(E)\left(\frac{m^*}{\pi\hbar^2(L_W + L_B)}\right)\exp\left(\frac{V_b^0 - qE\frac{L_W}{2} - (\varepsilon_1 + \varepsilon_F)}{kT}\right) \tag{5}$$

where k is the Boltzmann constant and T is the temperature. To calculate the dependence of the current density upon the donor concentration, the dependence of the activation energy $V_b^0 - (\varepsilon_1 + \varepsilon_F)$ upon the donor concentration for the QW of 5.7 nm width and the aluminum mole fraction in the barriers $x = 0.25$ was calculated by the nextnano program at T = 77 K. The doped middle part of the quantum well was 3.5-nm thick. The calculation results are shown in **Figure 5**.

As one can see from **Figure 5**, the barrier height decreases at the enhanced doping, which is caused by an increase in the Fermi level accompanied by an increase in the DEG concentration from 1.4×10^{11} to 3.4×10^{11} cm^{-2}.

Figure 6 shows the calculated dependences of the dark current density upon the applied electric field for different donor concentrations.

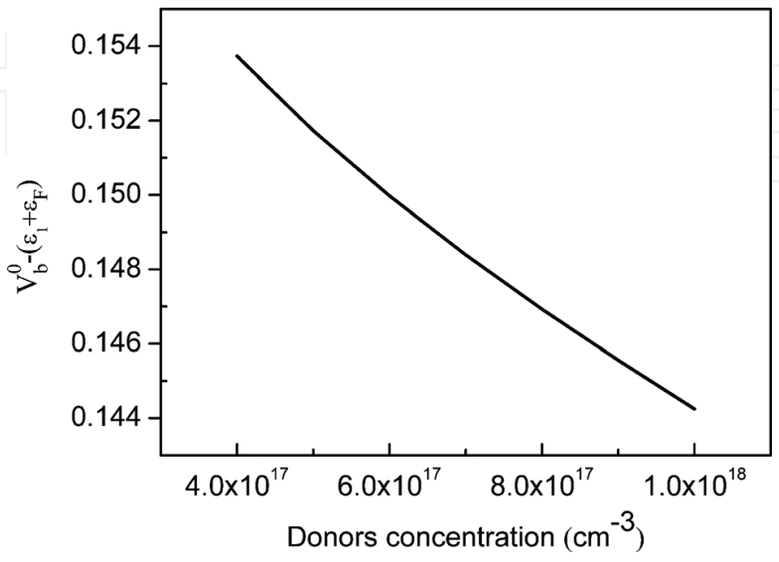

Figure 5. Dependence of the activation energy of the QWIP dark current upon the donor concentration.

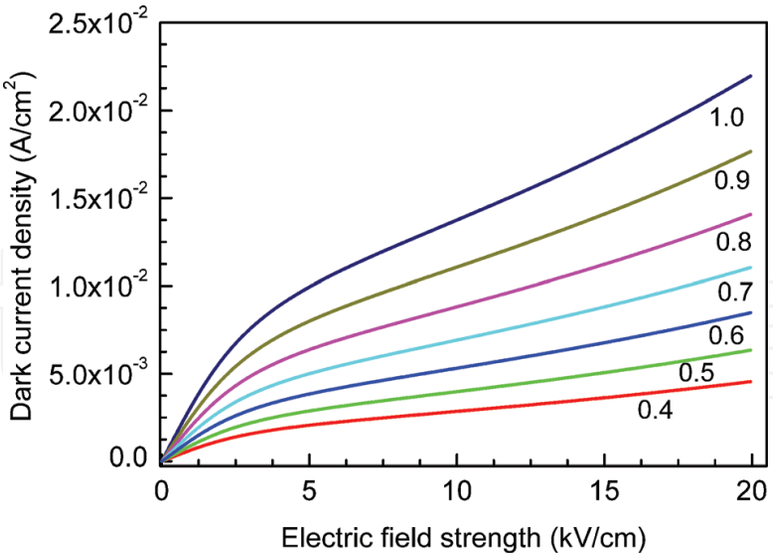

Figure 6. Dependence of the QWIP dark current upon the applied electric field for different donor concentrations. The donor concentration is indicated in units of 10^{18} cm^{-3} in the figure.

The optimum 2DEG concentration corresponding to the minimum value of the threshold power of the radiation (NEP) is estimated as follows. The value of NEP is given by:

$$NEP = \frac{I_n}{R} \tag{6}$$

where I_n is the noise current, R is the responsivity. The noise current depends on the dark current I_d as follows [10]:

$$I_n^2 = 4qg_n I_d \Delta f \tag{7}$$

where g_n is the coefficient of the noise gain and Δf is the width of the noise band. As one can see from the expression (Eq.(5)), the dark current increases exponentially at the increasing N_{2D}. Thus, for the degenerate 2DEG, the current depends on the 2DEG concentration N_{2D} (which is directly proportional to the donor concentration) as:

$$I_d \sim \exp\left(N_{2D}\pi\hbar^2/m^*kT\right) - 1 \tag{8}$$

In its turn, the responsivity is proportional to the absorption coefficient of a single QW α, which, in turn, is proportional to the DEG concentration [10]:

$$R \sim \alpha \sim N_{2D} \tag{9}$$

Thus, combining Eqs. (6)–(8), and Eq. (9), we obtain [11]:

$$NEP \sim \sqrt{e^{\rho}-1}/\rho \tag{10}$$

where $\rho = \pi^2 N_{2D}/m^*kT$. The minimum value of the expression given is achieved under the condition ϱ = 1.6 that is $N_{2D} = 2.7 \times 10^{11}$ or $N = 5.1 \times 10^{17}$ cm^{-3} for the quantum well of 5.3 nm width at the QWIP operating temperature of T = 70 K.

Thus, the maximum sensitivity of the GaAs/AlGaAs QWIP is expected to be around 8.6 μm to ensure the spectral range of the detector (8–10 μm). The calculations have shown that this condition is satisfied by such parameters of the doped QW as the well width L_W = 5.3 nm and aluminum mole fraction x = 0.25. When the ground state energy level is ε_1 = 66.8 meV, the energy of the first excited level is ε_2 = 206.0 meV, and the barrier height is V_b = 211.0 meV that corresponds to a fairly accurate coincidence of the first-exited quantum level and the edge of the potential barrier.

3. Properties of the heteroepitaxial GaAs/AlGaAs MQW structures

Multiple quantum wells GaAs/AlGaAs were obtained by the MBE on the GaAs (100) substrate with a buffer consisting of a 0.4-μm GaAs layer. The doped GaAs layers of 1.5 μm thickness were used as a base contact, whereas the upper ohmic contact was provided by the doped GaAs of 1.2 μm thickness.

It has been found that the best structural perfection of epitaxial GaAs layers and the greatest value of the carrier mobility can be obtained at a growth under conditions ensuring a (3 × 6) surface structure having a stoichiometric composition on the growth surface and being intermediate between the "As-stabilized" (2 × 4) and "Ga-stabilized" (4 × 2) surfaces. At the growth under such conditions, the concentrations of the gallium and arsenic vacancies on the surface are minimal, which provides a minimum concentration of the intrinsic point defects in the crystal. The deviation of the growth conditions toward the gallium or arsenic stabilization leads to the enrichment of the epitaxial layers by the defects of anion or cation sublattices, respectively. Since the (3 × 6) surface is observed in the narrow ranges of the substrate temperature and V/III flow ratio, the growth conditions around the transition from (2 × 4) to (3 × 6) surface can be recommended in order to obtain good process reproducibility.

Such growth conditions being applied, the necessary homogeneity and concentration of the growth defects across the wafer can be achieved. The distribution of the growth defect ("oval" defect) density is shown in **Figure 7**. One can see that the average density of the defects of 100–200 pcs/cm^2 can potentially lead to defectiveness of the photosensitive element matrix by no more than 0.2% (The number of pixels in the array of the photodetectors is 100–300 thousands). A small size of the growth defect in 4–6 microns suggests that even if one pixel is damaged, the neighboring pixels will remain unaffected.

The structure of the samples was examined by the method of studying the cross section of structures by the transmission electron microscopy (TEM). The studies were performed by the JEM-4000EX electron microscope by JEOL (Japan). The samples for the TEM were made in the geometry of the cross section by grinding them with their subsequent thinning during etching by Ar+ ions with an energy of 3–4 keV. The survey was conducted at an accelerating voltage of 400 kV. **Figure 8** shows the results of the TEM AlGaAs/GaAs heterostructure. The image represents no structural defects, which indicate a high quality of the heterostructures under study. The measurements carried out by the TEM methods demonstrate a good correspondence of the heterostructure layer thicknesses planned and obtained. Sharp changes in the

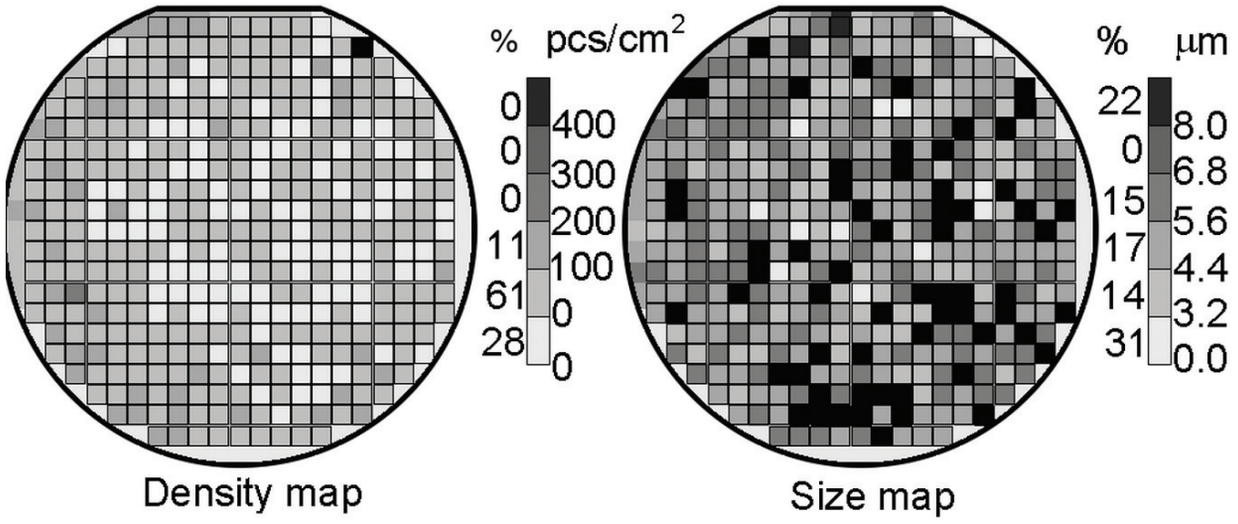

Figure 7. Distribution of surface defects of the epitaxial QWIP structure. The distribution of the density of defects (left) and defect sizes (right).

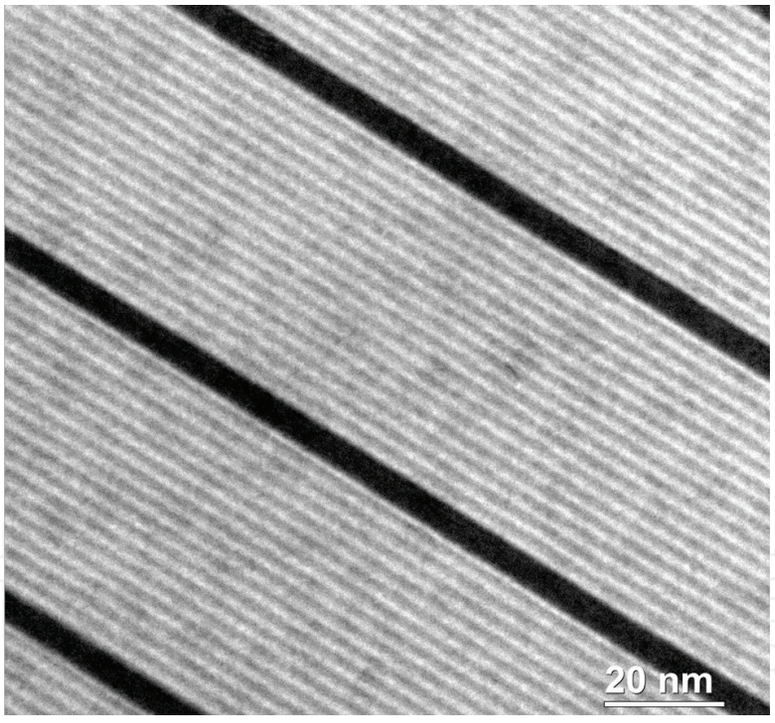

Figure 8. The cross section of the QWIP heterostructure.

intensity at the quantum well heterogeneities testify to fairly sharp and smooth transitions from one material to another.

The spectra of the piezomodulated reflection of the MQW structure in a visible spectral range at a liquid nitrogen temperature were measured to control the aluminum mole fraction in the AlGaAs barrier layers. Mechanical vibrations of the ceramic plate caused the modulation of the mechanical stresses in the structure, the modulations of the real $\Delta\varepsilon_r$ and the imaginary $\Delta\varepsilon_i$

parts of the dielectric constant, and as a consequence, the modulation of the reflection coefficient. The reflection variances ΔR are related to the variation of the dielectric constant by the Seraphin ratio [12]:

$$\frac{\Delta R}{R} = \alpha \Delta \varepsilon_r + \beta \Delta \varepsilon_i \tag{11}$$

where α and β are Seraphin coefficients. The energy position of the peaks in the piezoreflection spectrum corresponds to the electronic transitions in the structure under study. Typical piezoreflection spectra of the MQW structure are shown in **Figure 9A**. The aluminum mole fraction in the barrier layer is calculated from the peak energy. The peak at the 1.484 eV corresponds to the transitions from the levels of residual acceptors (neutral carbon atoms) to the conduction band in the GaAs substrate. The band gap of the GaAs at the 77 K is $E_g(GaAs) = 1.508$ eV [13], and the binding energy of the carbon atom is $\Delta = 25$ meV. Therefore, the calculated transition energy is expected to be $E_g(GaAs)$-Δ = 1.483 eV, which is in a good agreement with the experimental results. The peak at the 1.839 eV (or 674 nm) corresponds to the bound excitons in the $Al_XGa_{1-X}As$ barrier layers. The intermediate peaks between the 1.484 and 1.839 eV energies correspond to the transitions between the hole (light and heavy) and electron quantum levels in the MQWs [14]. Thus, the aluminum mole fraction in the barriers is determined from the energy position of the 1.839 eV line by a well-known relation between the bandgap width of the AlGaAs layer and the aluminum mole fraction (x) as $E_g(x) = E_g(0) + 1.427x + 0.041x^2$ [15].

The measurement of the QW width was carried out by means of the photoluminescence (PL) spectroscopy at a liquid nitrogen temperature along a line corresponding to the transition from the ground electron level to the ground level of the heavy holes *e1-h1*. According to calculations in the approximation of a rectangular quantum well of a finite depth for a quantum well with a width of 5 nm and an aluminum mole fraction of 0.26, the energies of the electron and

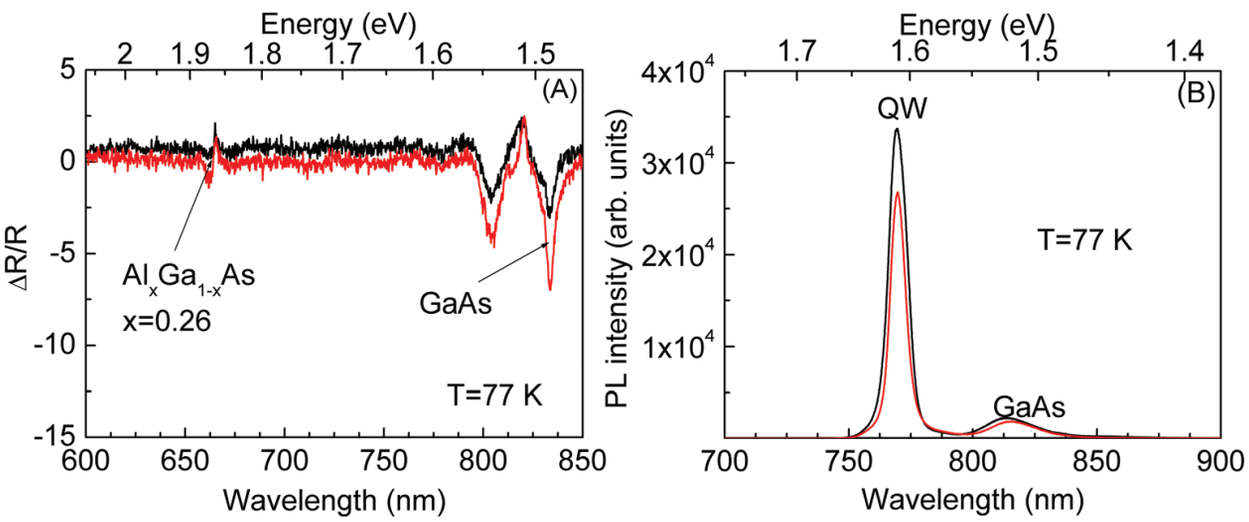

Figure 9. (A) The spectra of the piezomodulated reflection of the MQW structure. (B) The photoluminescence spectra of the MQW structure. The YAG laser was used to excite the PL.

hole ground quantum levels are 70 and 15 meV, respectively. Consequently, the energy of the *e1-h1* transition at a room temperature is expected about 1.6 eV. As one can see from **Figure 9B**, the measured maximum of the PL band *e1-h1* is located at 1.61 eV, which indicates the grown thickness of the layers being sufficiently accurate.

To control the electron concentration in the grown structures with MQWs, the C-V characteristics were measured. Those measurements were carried out with the specially fabricated Schottky barriers of the TiAu with a diameter of 200 μm and a C-V bridge operating at frequencies of 1 to 100 kHz. The upper contact layer had been previously etched and then measured. According to the measured C-V dependences, the concentration dependences upon the depletion region depth $N_{2D}(W)$ are determined from the relation:

$$N_{2D}(W) = {}^{2}/_{q\varepsilon}\varepsilon_0 S^2 \left(\frac{d(C^2)}{dV}\right)^{-1} \tag{12}$$

where q is the electron charge, C is the measured capacitance, V is the applied voltage, S is the area of the Schottky barrier, ε and ε_0 are the permittivity of the semiconductor and vacuum, respectively. The depth W, where the concentration of free carriers is determined, is $W = \varepsilon\varepsilon_0 S/C$, whereupon, the dependence of the sheet concentration with precision to constant upon the depletion region depth $\Delta\Gamma(W)$ was obtained by integrating $N_{2D}(W)$ (**Figure 10**). As one can see from the figure, all the experimental data obtained from different sample points agree with a high accuracy, which indicates a high uniformity of the electron density in the quantum wells over the wafer area. It should be noted that this method can be duplicated by a capacitive method where the mercury probe and profilometer operating at a frequency of 1 MHz are applied to measure the derivative.

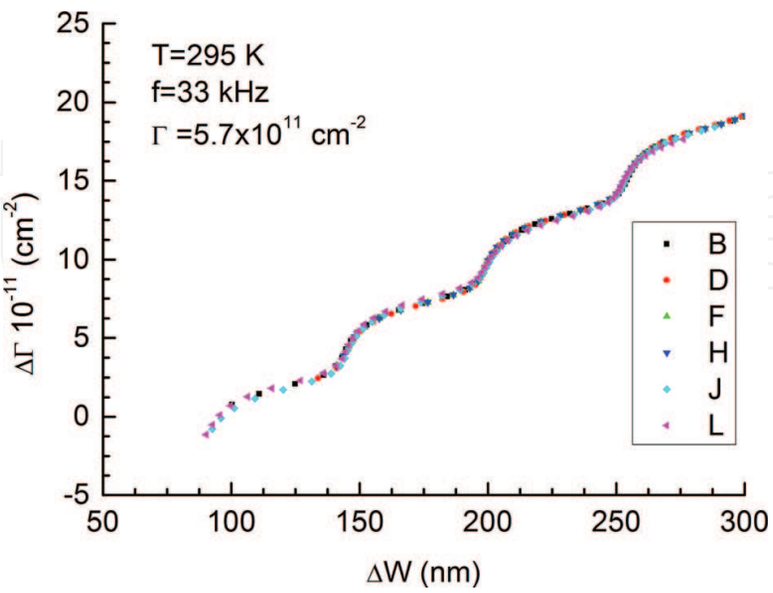

Figure 10. Distribution of the sheet concentration of the charge carriers ΔΓ in the quantum wells for six different points. These points are located along the wafer radius.

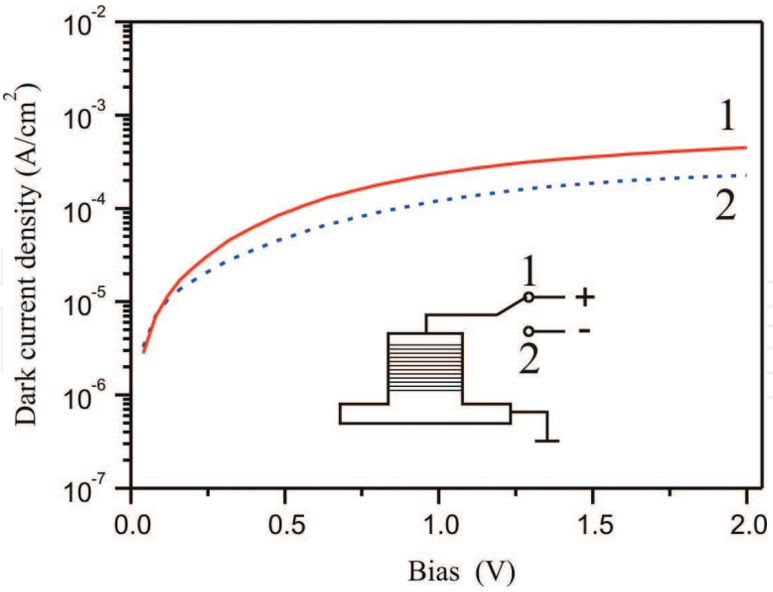

Figure 11. Field dependences of the dark current in the QWIP structure (the donor concentration is 2.5×10^{11} cm^{-2}) for various current directions at the 77 K temperature.

To calculate parameters of the multiplexer (capacitance and integration time), it is necessary to know the field dependences of the dark current. The measured dependencies of the dark current upon the bias for the QWIP structure made up of 30 periods of QW and barriers (L_b = 40 nm) with the pixel area 20 × 20 μm are presented in the **Figure 11**. As one can see from the figure, the current asymmetry is observed, which results from the segregation of the impurity atoms during the structure growth.

4. Selecting the parameters of the FPA on the basis of the GaAs/AlGaAs QWIP

While choosing a number of QW periods in the QWIP structure, the following must be taken into account: (A) an increase in a number of structure periods leads to an increase in the absorption coefficient, but, in turn, (B) the overall probability of capturing photoexcited electrons back into the QW, (C) the growth time of the heterostructure, (D) the mesa depth, and (E) the magnitude of the voltage applied to the structure increase as well. As a result, the sensitivity of the QWIP increases very weakly with an increasing number of the GaAs/AlGaAs layer periods [11]. Therefore, a heterostructure with 30 periods of the GaAs QW has been chosen.

A 2D diffraction grating with the parameters determined by the spectral range and properties of the dielectric applied is required to provide the absorption of a normal-incident light and increase the quantum efficiency of the QWIP [16]. The required etching depth of the lattice (d) is determined by the relation $d = \lambda/4n$, where λ is the radiation wavelength and n is the refractive index of the GaAs. These parameters are λ = 8–9 μm and d = 0.7–0.75 μm for the wavelength range applied. The period of the diffraction grating L = 2.8 μm was chosen so that the direction of the first diffraction order was an angle of 60° with the normal to the sample wafer.

The thickness of the upper contact layer of n+ doped GaAs was increased up to 1200 nm to adapt the fabrication technology for ohmic contacts. At a lower thickness of the contact layer, the metal may penetrate into the QW region as a result of diffusion during a long (5 minutes) annealing.

The multiplexer capacity and integration time of the signal were estimated by the dependency dark current upon the bias at the 77 K (**Figure 11**). The current at the bias voltage equal to 0.5 V is about 10^{-10} A, which, in the presence of the capacitance in the multiplexer equal to 6×10^6 electrons, allows integrating the signal during 10 ms.

5. The fabrication technology for the FPA on the basis of the GaAs/AlGaAs QWIP

The focal plane arrays on the basis of GaAs/AlGaAs QWIP structures were fabricated by the complex of coordinated technological operations based on photolithography processes using functional dielectric and metallic layers, etching processes, and chemical treatments of the heterostructures in the regimes determined by the physicochemical properties of the MQW layers. The technology development was carried out at the FPA with 384 × 288 elements with the 25 microns pitch. The structure control was carried out by the optical and scanning electron (LEO-1430, SU8220) microscopes.

5.1. Formation of the diffraction grating and mesa structure

A diffraction grating and mesa structures were formed by dry anisotropic etching of the GaAs layer in a remote gas-discharged plasma (ICP RF) of the BCl_3, argon, and nitrogen. The obtained diffraction grating holes are square shaped with rounded corners and vertical walls (**Figure 12A**). The view of the mesa structure walls formed by etching the GaAs at a given depth (2.4 μm) at the

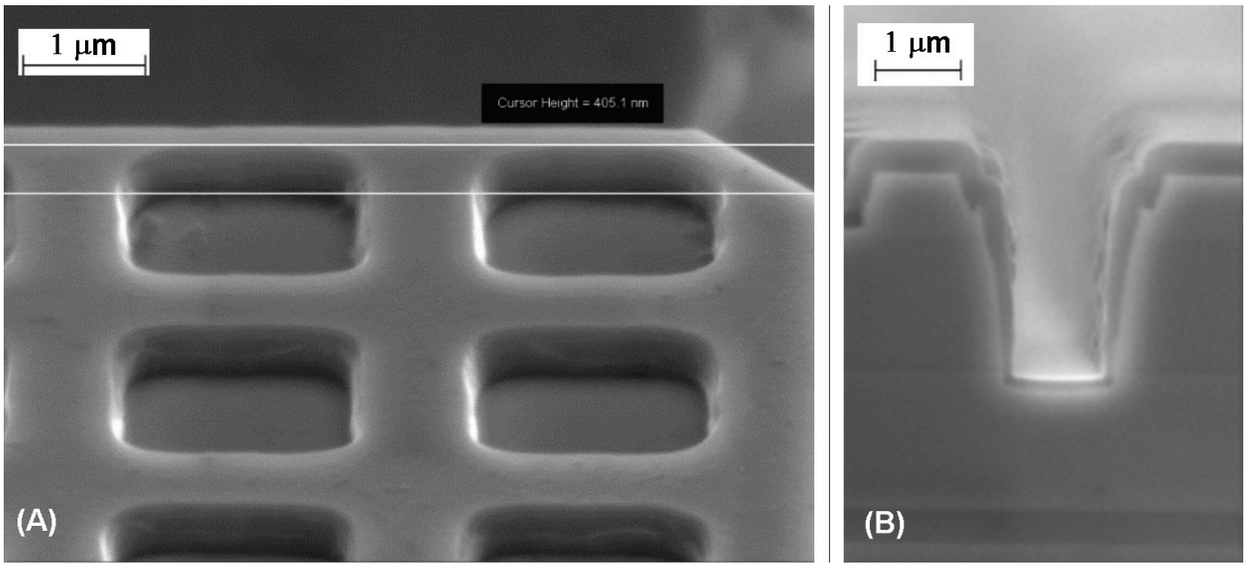

Figure 12. SEM images of (A) the diffraction grid and (B) the gap (2 μm) between the mesa structures of the FPA 384 × 288 elements obtained by dry etching with the 0.5-μm SiO_2 layer.

optimum ratios of reagent gases, the power of the RF and ICP generators, the reactor pressure, substrate temperature, heating, and etching time are shown in **Figure 12B.**

5.2. The fabrication of ohmic contacts

The ohmic contacts to the base and upper n+ doped GaAs layers (on the mesa surface) were fabricated by the Ge/Au/Ni/Au (20/20/20/100 nm) deposition [17] after the removal of the native oxide layer from the semiconductor surface by $HCl:H_2O$ (1:8) and annealing during 5 minutes at the 385°C in a hydrogen (**Figure 13**).

5.3. The mesa structure surface passivation

The SiO_2 dielectric layer was deposited by a low-pressure chemical vapor deposition (LP CVD) method at temperatures of 195–250°C to passivate and protect the mesa structure surface. The low temperature of this process excludes the disorder of the surface stoichiometric composition due to the evaporation at high temperatures of the fifth group element. Depending on the synthesis conditions, the layers of LP CVD SiO_2 (refractive index 1.46) have a dielectric constant of 5.9–6.5 and leakage currents of 6×10^{-8}–9×10^{-7} A/cm^2 ($E = 2 \cdot 10^6$ V/cm) at the room temperature with a water content of 2.5–3.3 volume percent, respectively. The SiO_2 formation at the semiconductor surface results in coating the vertical walls of the mesa structures (**Figure 12B**).

5.4. Production of indium bumps on the FPA and silicon multiplexers

To assemble a FPA by cold welding, indium bumps were fabricated both on the GaAs/AlGaAs QWIP structure and silicon multiplexers. The Tl xLift photoresist was used to produce indium bumps (height of ~5 μm) by inverse photolithography. The view and cleavage of a separate mesa

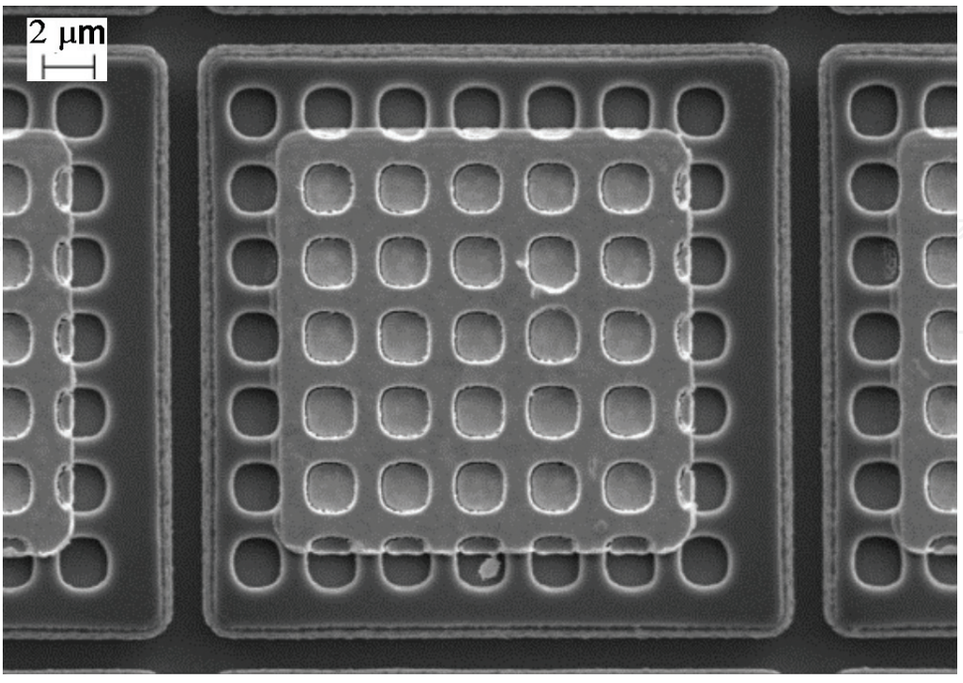

Figure 13. SEM image of the mesa structure of FPA 384 × 288 elements with a diffraction grating and the Ge/Au/Ni/Au (20/20/20/100 nm) metallization layer.

structure with an indium bump of the FPA of 384 ×·288 elements produced by the developed technology on the GaAs/AlGaAs heterostructures are shown in **Figure 14**.

5.5. Hybrid assembly of the FPA

The FPA modules were assembled by cold welding of the indium bumps under pressure [18]. The FPA and multiplexer crystals were docked on the M9 setup of Laurier company. The fusion of the indium contacts was performed by heating the module up to the indium melting temperature with the succeeding cooling. The surface autoplanarization is provided during the crystal compression process, which is achieved by installing polyamide stoppers along the perimeter of one of the module elements—an array or multiplexer. The maximum limit mechanical load is determined experimentally from the measurement of the curves of the plastic flow of the indium bumps, their height, and area. The pressure required for the plastic flow of the contacts ranges from 0.3 to 0.9 kg/mm^2. The total height of the indium bumps after the FPA assembly is 6–8 μm, which satisfies the requirements of the durability of the FPA hybrid assemblies [19].

5.6. The GaAs substrate removal from the FPA assembly

The technology of the substrate removal after the assembly of the FPA consisted of the successive processes of the mechanical grinding aimed at removing the main thickness of the GaAs substrate, chemical mechanical polishing and chemical dynamic polishing, in order to obtain a mirror-smooth surface of the array crystal. The processes of the chemical selective etching of the GaAs and heterostructure layers were applied to remove the GaAs substrate from the FPA surface completely (**Figure 15**) [20–22].

5.7. Technical characteristics of the multiplexer

The silicon multiplexers by Integral Joint Stock Company (IZ640FD format 640 × 512) made by the CMOS technology and meeting the QWIP requirements were used as a part of the FPA assembly [23].

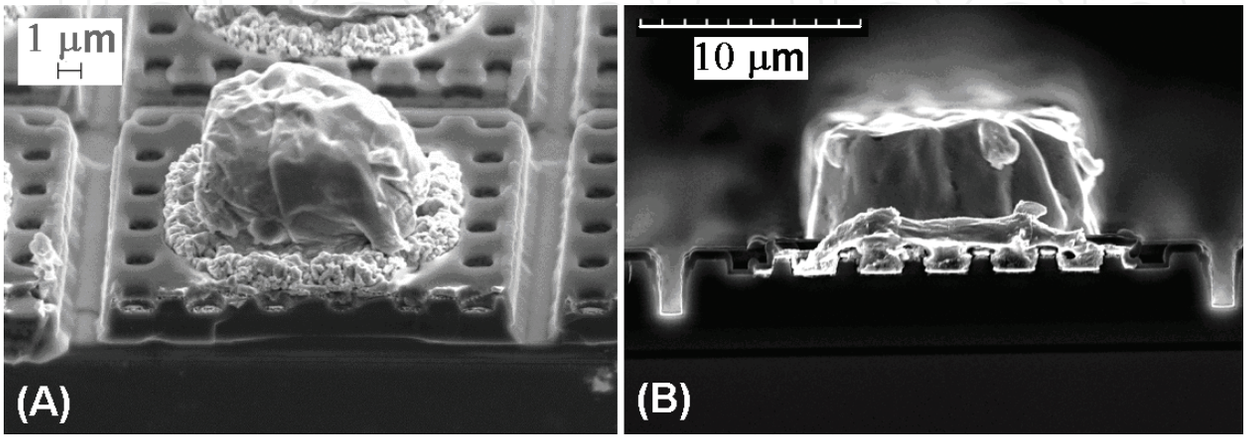

Figure 14. SEM images (A) of the mesa structure and (B) mesa structure cleavage of the FPA with 288 × 384 pixels on the basis of GaAs/AlGaAs QWIP structures with indium bumps.

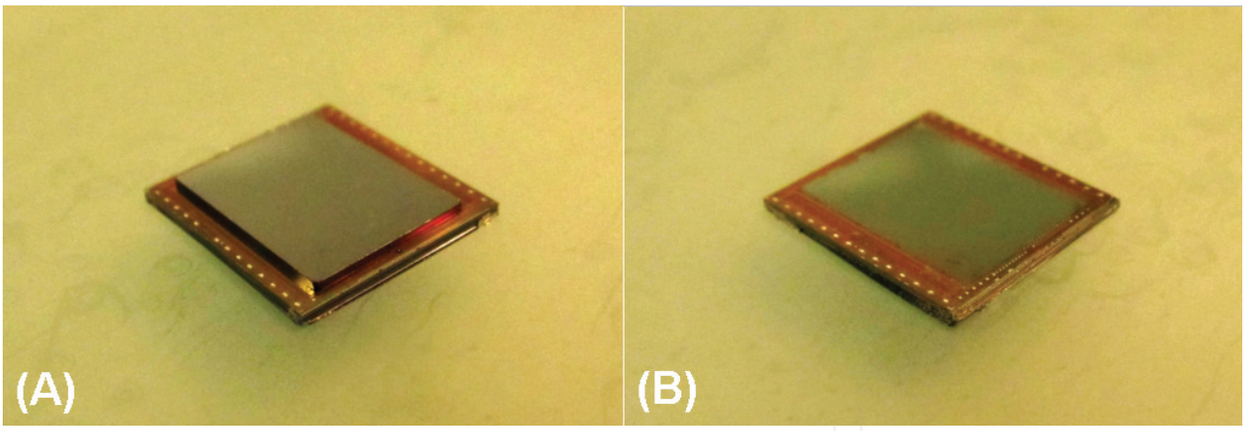

Figure 15. The photo of the FPA assembly with 384 × 288 elements (A) before and (B) after the removal of the GaAs substrate (650 μm).

The storage capacitance in every cell of the IZ640FD multiplexer was approximately 8×10^6 electrons with a reading noise of 1000 electrons. The adjustable integration time could vary from 100 microseconds to the entire duration of the frame scanning. The electric power consumed at a frame rate of 100 Hz did not exceed 120 mW. The electric power consumed at a frame rate of 100 Hz did not exceed 140 mW in the four output mode and 90 mW at a switch into one output mode, respectively.

The schematic diagram of the input block of the multiplexer is shown in **Figure 16**, where D is the photoresistor (detector), VD is the detector supply voltage, VB is the voltage specifying the detector bias voltage, VA is the voltage specifying the level of anti-burglary, VS is the skimming voltage, C1 is the integration capacitance in pixel, C2 is the storage capacity in pixel, C3 is the storage capacity in column, K1, K2, and K3 are the keys, A is the amplifier with a controlled gain, and B is the buffer. The signal integration occurs simultaneously on all the array elements, and then, the voltage from the capacitances C2 is line-by-line read out by connecting the key K2 to the column capacitance C3 and the column amplifier A.

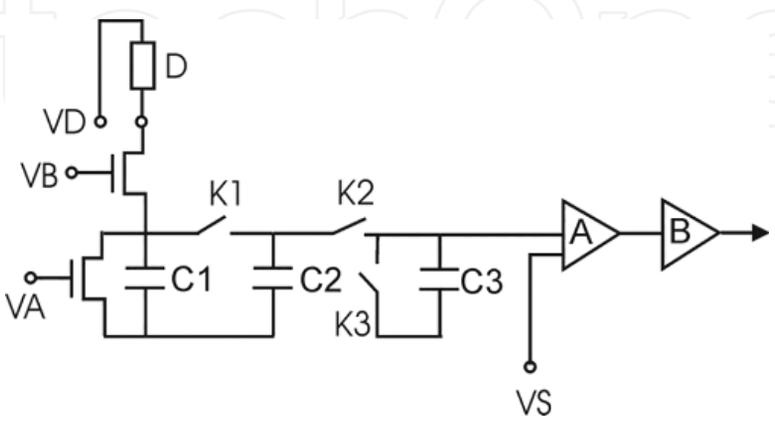

Figure 16. Schematic diagram of the input multiplexer for the FPA.

6. Opto-electronic characteristics of the FPA assembly

At the final stage, the opto-electronic characteristics of the fabricated FPA assembly were determined. For this purpose, the assembly was placed in a nitrogen cryostat with an entrance window made of the ZnSe. The operating temperature of 65 K was achieved due to the pressure pumped down by a vacuum pump. A cooled diaphragm provided a relative aperture of 1:2. To measure the sensitivity of the FPA, the module illumination was made by an extended-type absolutely black body. It should be noted that the high parameters of the FPA assembly both the absolute values of the signals and their homogeneity with respect to the array elements are supposed to be essential.

The distribution histogram of the total current (dark + photo signal from the 300 K background) for the FPA assembly thinned up to 170 μm is shown in **Figure 17A**. The integration time of the signal was chosen to be 9 ms. **Figure 17B** shows the distribution histogram of the temperature sensitivity of the S_T at the 300 K background upon the pixels of the FPA module BM20. Its average value is rather high and equal to 23.2 mV/K. **Figure 17C** shows

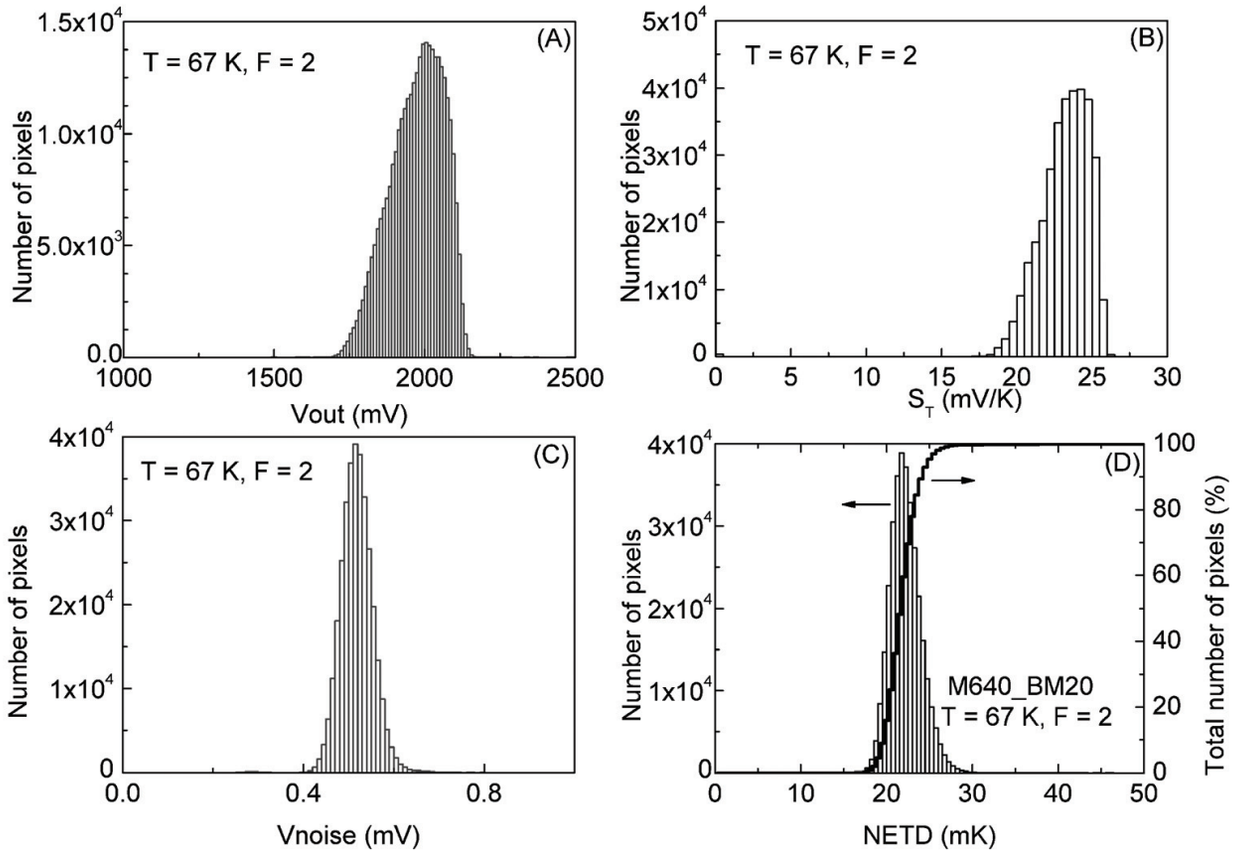

Figure 17. (A) The histogram of the total current distribution of the 640 × 512 FPA module BM20. (B) The histogram of the temperature sensitivity at a background of 300 K of the 640 × 512 FPA module BM20. (C) The histogram of the noise voltage of the 640 × 512 FPA module BM20. (D) Experimentally measured NEΔT histogram of the 640 × 512 FPA module BM20.

the distribution of the noise voltage V_n at the output of the photoreceptor module BM20 at a background of 300 K. All the histograms are rather narrow, which demonstrates the high uniformity of the array parameters. The noise equivalent temperature difference NETD = V_n/S_T of the FPA module BM20 is shown in **Figure 17D**. The average value of a NETD for nondefective pixels at the FPA temperature of 67 K is 22.2 mK. A number of defective elements with a NETD over 70 mK is 0.15%. A typical spectrum of photosensitivity of a 640 × 512 FPA is shown in **Figure 18**. An example of the IR image detected by a

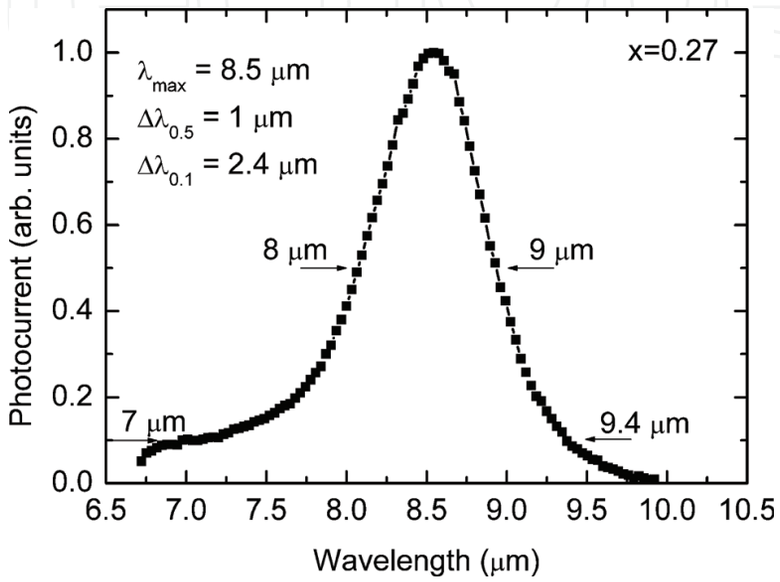

Figure 18. Photosensitivity spectrum of the FPA.

Figure 19. The example of an IR image. The temperature is 65 K. The integration time is 6 ms. The working elements are 99.6%.

640 × 512 FPA assembly module equipped by the germanium lens with D/F = 1:2 aperture is shown in **Figure 19**.

The developed technology for the FPA assembly is reproducible and has a rather high yield percentage of the suitable products well seen from **Figure 20** showing the scatter of the noise equivalent temperature differences and a number of defective elements for the 640 × 512 FPA assembly manufactured on the 5 MBE grown heterostructures.

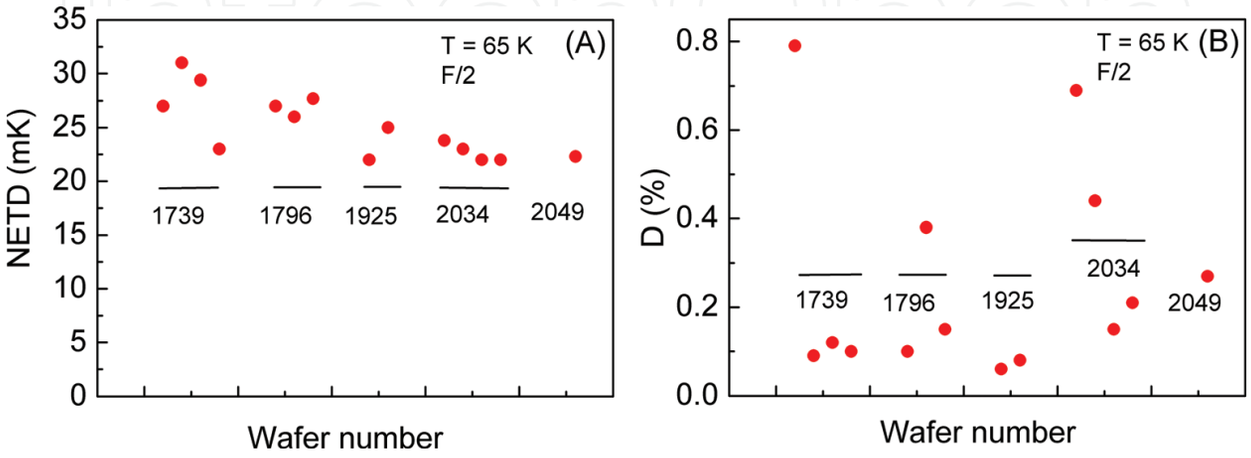

Figure 20. (A) Scatter of NETD and (B) a number of defective elements in the 640x512 FPAs produced on the five grown QWIP structures.

Figure 21. The photo of the QWIP IDCA.

	ISP SB RAS (Russia) BM20	**Sofradir (France) SIRIUS-LW**
Array format	640 × 512	640 × 512
Pixel pitch, μm	20	20
Peak sensitivity, μm	8.5–8.6	8.5
FWHM, μm	0.8–1	1
NETD, mK	<35	<35
Operability, %	>99.5	99.9%
Integration time, ms	6	7
Operating temperature, K	72	70–73

Table 1. Comparative characteristics of the GaAs/AlGaAs QWIP IDCA by the ISP of the SB RAS (Novosibirsk) and Sofradir (France).

6.1. Integrated detector cooler assembly

The fabricated and tested 640 × 512 FPA were installed in the body of a vacuum cryostat integrally coupled with a microcryogenic system. Resulted integrated detector cooler assembly (IDCA) is showed in **Figure 21**. A vacuum cryostat performs thermal isolation of the array from the environment to guarantee effective cooling of the photodetector up to the operating temperature (T = 68–72 K). The radiation from the detected objects is fed to the FPA through an input window made up of the germanium with the antireflection in the range of 8–10 μm and a cooled diaphragm with a relative aperture F/2 designed to reduce the background illumination. A low pressure in the vacuum cryostat is provided by a getter, whose reactivation is carried out by passing an electric current through it. Typical operating temperatures for the FPA based on the QWIP with the wavelength range 8–10 μm are 68–72 K. Thus, the powerful microcryogenic systems ensuring a cooling capacity at an operating temperature of 70 K not less than 0.4 W and the power consumption not more than 20 W are needed to provide the required temperature in a full range of climatic conditions.

As one can see from **Table 1**, the parameters of the developed 640 × 512 QWIP IDCA are comparable with those of the Sofradir products.

7. Conclusions

The technology of manufacturing the AlGaAs/GaAs QWIP FPA has been discussed. The parameters of a FPA of 640 × 512 format with a 20-μm pitch for a spectral range of 8–10 μm have been described. At an operating temperature of 72 K, the temperature resolution of the QWIP FPA is less than 35 mK. The frame rate is 100 Hz. A number of defect elements in the array do not exceed 0.5%. It is shown that the parameters of the QWIP FPA fabricated by Rzhanov Institute of Semiconductor Physics of SB RAS meet the world class standards.

Author details

Michael A. Dem'yanenko, Dmitry G. Esaev, Aleksandr I. Toropov, Natalia A. Valisheva, Sergey A. Dvoretsky, Dmitry V. Dmitriev, Dmitry V. Gulyaev, Vladimir A. Fateev, Igor V. Marchishin, Dmitry Yu Protasov, Anatoly P. Savchenko, Victor N. Ovsyuk and Konstantin Zhuravlev*

*Address all correspondence to: zhur@isp.nsc.ru

Rzhanov Institute of Semiconductor Physics of SB RAS, Novosibirsk, Russia

References

[1] West LC, Eglash SJ. First observation of an extremely large-dipole infrared transition within the conduction band of a GaAs quantum well. Applied Physics Letters. 1985;**46**:1156. DOI: 10.1063/1.95742

[2] Levine BF, Choi KK, Bethea CG, Walker J, Maliл RJ. New 10 μm infrared detector using intersubband absorption in resonant tunneling GaAlAs superlattices. Applied Physics Letters 1987;**50**:1092. DOI: http://dx.doi.org/10.1063/1.97928

[3] Rafol SB, Cho E, Lim W. Characterization of very large format 1K×1K LWIR QWIP focal plane array. Proceedings of SPIE. 2007;**6678**:6678X-1. DOI: http://dx.doi.org/10.1117/12.736137

[4] Robo JA, Costard E, Truffer JP, Nedelcu A, Marcadet X, Bois P. QWIP focal plane arrays performances from MWIR up to VLWIR. Proceedings of SPIE. 2009;**7298**:72980F-729801. DOI: http://dx.doi.org/10.1117/12.820470

[5] Reibel Y, Rubaldo L, Manissadjian A, Billon-Lanfrey D, Rothman J, de Borniol E, Destéfanis G, Costard E. High-performance MCT and QWIP IR detectors at Sofradir. Proceedings of SPIE. 2012;**8541**:85410A. DOI: http://dx.doi.org/10.1117/12.975671

[6] Gunapala SD, Bandara SV, Liu JK, Mumolo JM, Rafol SB, Ting DZ, Soibel A, Hill C. Quantum well infrared photodetector: Technology and applications. IEEE Journal of Selected Topics in Quantum Electronics. 2014;**20**(6):3802312. DOI: 10.1109/JSTQE.2014.2324538

[7] Martijn H, Gamfeldt A, Asplund C, Smuk S, Kataria H, Costard E. QWIPs at IRnova, a status update. Proceedings of SPIE. 2016;**9819**:981918. DOI: http://dx.doi.org/10.1117/12.2228348

[8] Davies JH. The Physics of Low-Dimensional Semiconductors: An Introduction. Cambridge: Cambridge University Press; 1998. 438 p

[9] Nextnano. Software for semiconductor nanodevices [Internet]. 2017. Available from: www.nextnano.de [Accessed: 2017-10-25]

[10] Schneider H, Liu HC. Quantum Well Infrared Photodetectors: Physics and Applications. Heidelberg: Springer; 2007. 248 p. DOI: 10.1007/978-3-540-36324-8

[11] Levine BF. Quantum well infrared photodetectors. Journal of Applied Physics. 1993;**74**(8): R1. DOI: http://dx.doi.org/10.1063/1.354252

[12] Seraphin O, Bottka N. Band-structure analysis from electro-reflectance studies. Physical Review. 1966;**145**:628. DOI: https://doi.org/10.1103/PhysRev.145.628

[13] Lee YR, Ramdas AK, Moretti AL, Chambers FA, Devane GP, Ram-Mohan LR. Piezomodulated reflectivity spectra of GaAs/AlGaAs single-parabolic-quantum-well heterostructures. Physical Review B. 1990;**41**:8380. DOI: https://doi.org/10.1103/PhysRevB.41.8380

[14] Vurgaftman I, Meyer JR, Ram-Mohan LR. Band parameters for III-V semiconductors and their alloys. Journal of Applied Physics. 2001;**89**:5815. DOI: http://dx.doi.org/10.1063/1.1368156

[15] Pollak FH, Shen H. Modulation spectroscopy characterization of MOCVD semiconductors and semiconductor structures. Journal of Crystal Growth. 1989;**98**:53. DOI: 10.1016/0022-0248(89)90185-1

[16] Anderssen JY, Lundqvist L and Paska ZF. Grating-coupled quantum–well infrared detectors: Theory and performance. Journal of Applied Physics 1992;**71**:3600. DOI: http://dx.doi.org/10.1063/1.350916

[17] Baca AG, Renb F, Zolpera JC, Briggsa RD, Peartonc SJ. A survey of ohmic contacts to III-V compound semiconductors. Thin Solid Films. 1997;**308-309**:599. DOI: 10.1016/S0040-6090(97)00439-2

[18] Klimenko AG, Voinov VG, Novoselov AR, Nedosekina TN, Vasilyev VV, Zakhariash TI, Ovsyuk VN. Soft indium bumps for indium bump bonding FPAs on CdHgTe. Optoelectronics Instrumentation and Data Processing C/C of Avtometriia. 1998;**4**:87

[19] Smith HI. Fabrication techniques for surface-acoustic-wave and thin-film optical devices. Proceedings of the IEEE. 1974;**62**:1361. DOI: 10.1109/PROC.1974.9627

[20] Zhao R, Lau WS, Chong TC, Li MF. A comparison of the selective etching characteristics of conventional and low-temperature-grown GaAs over AlAs by various etching solutions. Japanese Journal of Applied Physics. 1996;**35**:22. DOI: https://doi.org/10.1143/JJAP.35.22

[21] Spooner F, Quinn W, Hanes L, Woolsey S, Smith K, Maison J. A reproducible, high yield, robust wet etch etch-stop process using organic acid – peroxide solutions. [On-line Digest Table. The International Conference on Compound Semiconductor Manufacturing Technology (Sharing Ideas Throughout the Industry)]. [Internet]. Available from: http://csmantech.org/OldSite/Digests/2004/2004Papers/8.9.pdf [Accessed: 25 Oct 2017]

[22] Chang EY, Lai Y-L, Lee YS, Chen SH. A GaAs/AlAs wet selective etch process for the gate recess of GaAs power metal-semiconductor field-effect transistors. Journal of the Electrochemical Society. 2001;**148**:G4. DOI: 10.1149/1.1344555

[23] "INTEGRAL" Joint Stock Company [Internet]. Available from: HYPERLINK "http://www.integral.by/en" www.integral.by/en [Accessed: Oct 25, 2017]